Molecular dynamics simulations of hcp/fcc nucleation and growth in bcc iron driven by uniaxial compression

2009 J. Phys.: Condens. Matter 21 495702

(http://iopscience.iop.org/0953-8984/21/49/495702)

J. Phys.: Condens. Matter **21** (2009) 495702 (6pp) doi:10.1088/0953-8984/21/49/495702

Molecular dynamics simulations of hcp/fcc nucleation and growth in bcc iron driven by uniaxial compression

B T Wang[1,2], J L Shao[2], G C Zhang[2], W D Li[1] and P Zhang[2,3]

[1] Institute of Theoretical Physics and Department of Physics, Shanxi University, Taiyuan 030006, People's Republic of China
[2] LCP, Institute of Applied Physics and Computational Mathematics, Beijing 100088, People's Republic of China
[3] Center for Applied Physics and Technology, Peking University, Beijing 100871, People's Republic of China

E-mail: zhang_ping@iapcm.ac.cn

Received 17 September 2009, in final form 28 October 2009
Published 12 November 2009
Online at stacks.iop.org/JPhysCM/21/495702

Abstract

Molecular dynamics simulations have been performed to study the structural transition in bcc iron under uniaxial strain loading. We found that the transition pressures are less dependent on the crystal orientations, ∼14 GPa for [001], [011], and [111] loadings. However, the pressure interval of a mixed phase for [011] loading is much shorter than loading along other orientations. In addition, the temperature increased amplitude for [001] loading is evidently lower than other orientations. The nucleation and growth of the hcp/fcc phases, and their crystal orientation dependence, were analyzed in detail, where the atom structure was presented by the topological medium-range-order analysis. For [001] compression, the hcp structure occurs first and grows into a laminar morphology in the $(011)_{bcc}$ plane with some fcc atoms as an intermediate structure. For loading along [011] and [111] directions, both hcp and fcc structure nucleation and growth along the $\{110\}_{bcc}$ planes are observed; their morphology is also discussed.

(Some figures in this article are in colour only in the electronic version)

1. Introduction

The structural phase transition is an important physical phenomenon in solid materials under high pressure, particularly in metallic systems. Iron is one kind of typical transition metals, and the transition pressure was discovered at around 13 GPa by Bancroft *et al* [1] in 1956. In 1962, Jamieson and Lawson proved by static x-ray diffraction experiments [2] that the above transition is the bcc to hcp transition. Due to its critical importance in condensed-matter physics, materials science, geophysics [3–5], and human development, much theoretical and experimental work has been done to study iron's bcc to hcp transition properties [4, 6–10]. Among these studies, Taylor and Pasternak reported the onset of the transition in range of 9–15 GPa with a large hysteresis width of about 6 GPa [6]; Boettger and Wallace presented a theoretical analysis of metastability and dynamics of the transition [8]; Wang and Ingalls suggested three possible models for the bcc to hcp transition mechanism [9]; and Caspersen *et al* theoretically investigated the influence of shear in the transition based on a multiscale model [10].

However, the structural transition is a mutation process, which makes direct observation of the phase transition very difficult in experiment. The abrupt changes in physical and mechanical characteristics also bring about difficulty in theoretically analyzing the dynamic response and micro-behavior of the materials. Therefore, it is necessary to carry out systematic simulations at the atomic level by using molecular dynamics (MD). In recent years, many simulation works have been focused on the structural transition of iron. For example, in 2002, Kadau *et al* [11] realized the micro-simulation of a shock-induced phase transition of bcc iron with an embedded atom method (EAM) potential [12, 13], showing the micro-mechanism of the bcc to hcp transition. A subsequent ultrafast

x-ray diffraction experiment processed by Kalantar *et al* [14] verified the validity of this work. In 2005 and 2007, Kadau *et al* [15, 16] reported the orientation dependence of the microstructure on the crystallographic shock direction and the simulations on the polycrystal iron under shock loading. It was found that the fcc phase can form in single crystal iron by uniaxial loading along [011] and [111] directions, or in polycrystal iron.

These above mentioned MD studies have greatly enriched our knowledge of the structural transition of iron and, needless to say, inspired the subsequent simulation work [17, 18]. In our last work [18], we have simulated the bcc to hcp structural transition of iron under isothermal compression along the [001] direction. We showed the formation process of a laminar structure along the $\{110\}_{\mathrm{bcc}}$ planes and the dynamics properties. On the other hand, both hcp and fcc nucleation and growth in bcc single crystal iron will occur for the [110] and [111] loadings. Thus, how the hcp/fcc nucleates and evolves is an important problem in understanding the structure of iron. In this paper, we present the simulations on the hcp/fcc nucleation and growth by adiabatic compression along [001], [011], and [111] directions, respectively. We show in detail the micro-dynamics for different directions of compression by the topological medium-range-order analysis.

2. Methodology of the simulations

For this work, we used the EAM potential of iron developed by Voter–Chen (VC) [19], which has been used in simulating the phase transition of iron in many previous works [11, 15, 16, 18], to conduct the simulations. Our calculations were performed in three cases by using three samples A, B, and C to simulate the loadings along the [001], [011], and [111], respectively. Sample A consists of $50_{x,[100]} \times 50_{y,[010]} \times 100_{z,[001]}$ atomic cells, sample B consists of $36_{x,[011]} \times 100_{y,[\bar{1}00]} \times 72_{z,[0\bar{1}1]}$ cells, and sample C consists of $36_{x,[\bar{1}10]} \times 40_{y,[\bar{1}\bar{1}2]} \times 180_{z,[111]}$ cells. Periodic boundary conditions were adopted in all the directions. The original temperature in all samples was set at 60 K by the speed calibration method [20]. The compressive stress tensor was calculated according to the virial formula [21, 22]:

$$p_{\alpha\beta} = \frac{1}{V}\Big(\sum_i m_i v_{i\alpha} v_{i\beta} + \sum_i \sum_{i>j} r_{ij\alpha} f_{ij\beta}\Big), \qquad (1)$$

where the summation is over all atoms and $\alpha(\beta)$ represent x, y or z axes. The first term in the stress tensor is the momentum flow of atom i and the second term is the microscopic virial potential stress. The initial state was manipulated at zero pressure through modulating the lattice constant. Here the lattice constant of all samples is $a_0 = 0.28725$ nm. This simulation is a NVE ensemble. However the volume varies at every step, which is different from quasistatic compression. Loading with a high strain rate of $\sim 10^8$ along the [001], [011], and [111] directions was implemented by shortening the lattice constants of these three orientations step by step during the MD process. The Verlet algorithm [23] was used to integrate the equation of motion. The simulation time was up to 200 ps, with a time step of 2 fs. Analyzing the huge amount of data produced in the MD simulations requires special techniques. Here, the local structure around each atom was resolved by using the topological medium-range-order analysis [24] technique. The phase mass fraction analysis and radial distribution function were also presented to obtain the phase transition information.

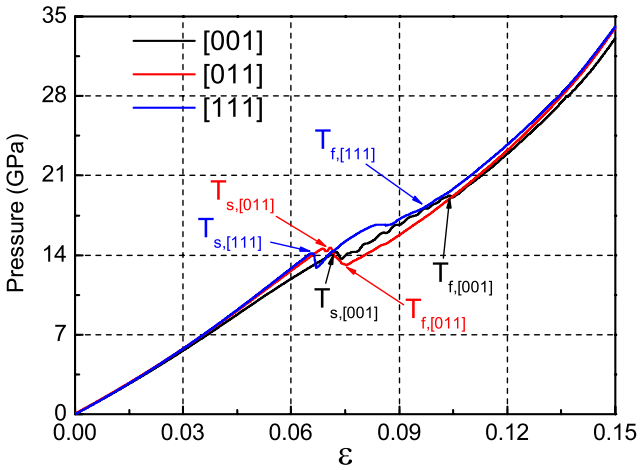

Figure 1. Variation of pressure with the strain ε for loading along [001], [011], and [111] directions. The mixed phase intervals start at $T_{\mathrm{s},[001]}$ (0.072, 14.21), $T_{\mathrm{s},[011]}$ (0.071, 14.66), and $T_{\mathrm{s},[111]}$ (0.066, 14.16) and finish at $T_{\mathrm{f},[001]}$ (0.104, 19.25), $T_{\mathrm{f},[011]}$ (0.075, 13.17), and $T_{\mathrm{f},[111]}$ (0.097, 18.28) for [001], [011], and [111] loadings, respectively.

3. Results and discussion

3.1. Pressure and temperature effects

To begin with, we perform the pressure analysis during the loading process. The calculated pressure as a function of compression strain ε is shown in figure 1, where $\varepsilon = 1 - V/V_0$ and V_0 is the initial volume of the samples. With increasing compression strain, the following prominent features can be seen from figure 1: (i) the transition critical points in the strain–pressure space are $T_{\mathrm{s},[001]}$ (0.072, 14.21), $T_{\mathrm{s},[011]}$ (0.071, 14.66), and $T_{\mathrm{s},[111]}$ (0.066, 14.16) for loading along [001], [011], and [111] directions, respectively, which illustrates that the critical pressures of transition are less dependent on the crystal orientations. This conclusion is similar to the shock-loading simulations by Kadau *et al* [15]. However, the strain threshold for [111] compression is evidently lower than the others, suggesting that sample C needs less compression to begin transition. After the critical points the pressure is lowered due to the hcp/fcc nucleation in the metastable state; (ii) the pressure–strain curve for [001] loading is below the other two curves prior to the transition, which indicates that samples B and C experience a more evident hardening process than sample A; (iii) the mixed phase intervals for loading along [001], [011], and [111] directions are different, where the mixed phase interval for [011] loading is very much shorter than [001] and [111] loadings. This is due to the fact that the compression direction in sample B is parallel to the nucleation

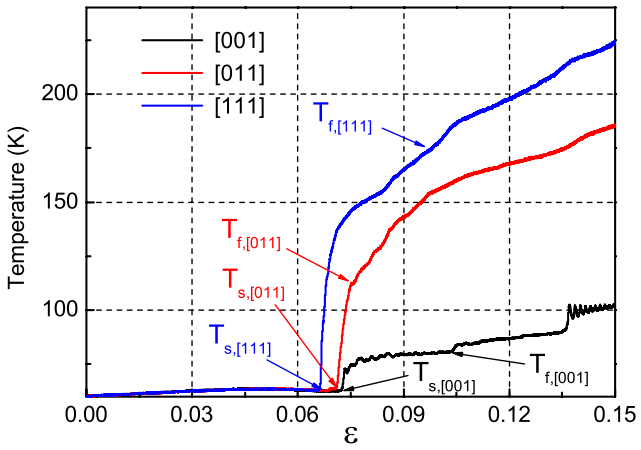

Figure 2. Variation of temperature with the strain ε for loading along [001], [011], and [111] directions. The letters $T_{s,i}$ and $T_{f,i}$ (i stands for [001], [011], and [111]) have the same strains as that in figure 1.

planes (see below for further discussion). Note that the criteria used to determine the transition finish (T_f) points can be viewed from figure 3. When the mass fraction of close packed phases (both fcc and hcp) is over 0.7, we confirm that the transition process is finished.

The temperature evolution with the strain is presented in figure 2. One can see that the temperature values at the three starting transition critical points (namely, $T_{s,[001]}$, $T_{s,[011]}$, and $T_{s,[111]}$) are all near 64 K, however, the nucleation under three loading directions displays remarkably different temperature effects. The temperature is progressively higher with a sequence of [001] (∼102 K), [011] (∼185 K), and [111] (∼223 K) loadings. In addition, the temperature increase style is different. The temperature of sample A increases in an upwardly stair-like manner, which can be seen more clearly near the labels $T_{s,[001]}$ (0.072, 63.63), $T_{f,[001]}$ (0.104, 81.17), followed by a sawtooth-like slope after exceeding a strain of 0.136. These features of temperature in sample A have not been observed in samples B and C. Instead, the temperatures in samples B and C first alter suddenly up to 110 and 142 K from the initial value of ∼64 K, respectively in 5.3 and 9.3 ps. Then they increase steadily with strain. On the whole, the remarkable distinction in temperature before and after phase transition illustrates a substantial structural and energetic complexity during transition process.

3.2. Nucleation and growth of hcp and fcc phases

The transformation mechanism can be described as being that the adjacent (110) or $(1\bar{1}0)$ faces shuffle relatively along the $[1\bar{1}0]$ or [110] directions after the sample has contracted (along the [001] direction) to a critical value [11, 25]. Here, we mainly explore in detail the process of nucleation and growth of new phases. Figures 3(a)–(c), respectively, show the mass fraction λ for the hcp and fcc phases during their evolution with the loading strain along the three directions. Obviously, while most atoms in sample A nucleate into the hcp structure, in samples B and C there will emerge a near half proportion of fcc atoms. This is similar to the observation in the shock-wave loading simulation [16], where it was found that the hcp/fcc

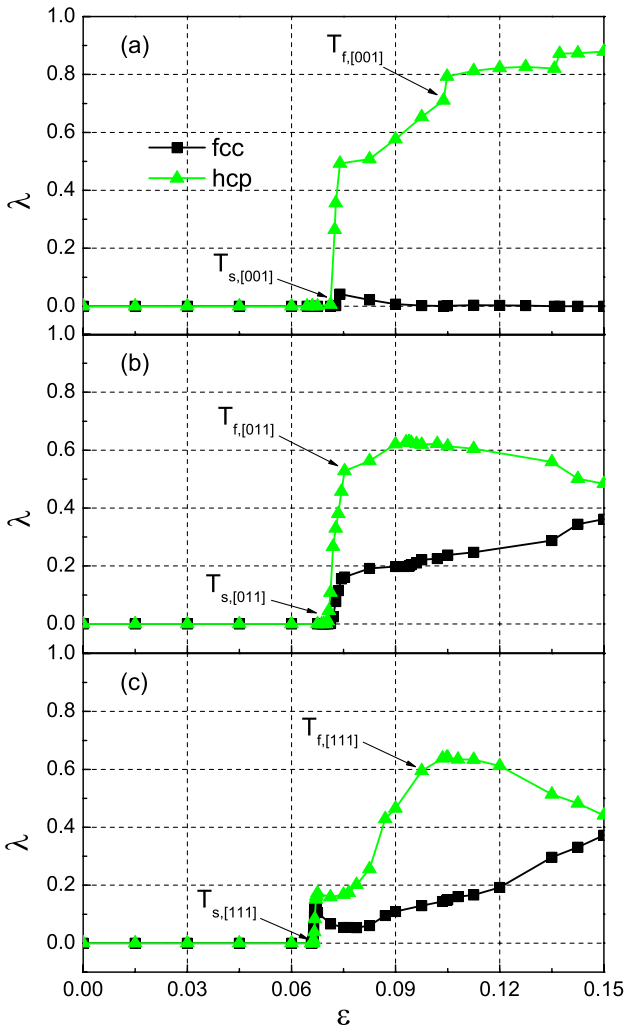

Figure 3. Mass fractions λ for the fcc and hcp phases change with strain ε for loading along [001] (a), [011] (b), and [111] (c) directions.

ratio within a grain decreases the more the shock direction deviates from the $[001]_{bcc}$ direction of the initial polycrystal. Our results also show that, with the pressure increasing, more fcc atoms will form when loading along the [011] and [111] directions.

The dynamic properties of the bcc to hcp transition under [001] compression have been investigated in [18]. Here, we focus on the emergence and growth of both hcp and fcc phases when compression is along different directions. Over the critical pressure, the microscopic view of the initial nucleation and growth of the fcc (upper panels) and hcp (lower panels) phases for samples A, B, and C are shown in figures 4–6, respectively.

The case of [001] loading is shown in figure 4. One can see some fcc phase atoms in the mixed phase interval, nucleating on the $(\bar{1}10)_{bcc}$ plane, while the fcc atoms either transform to hcp or becomes grain boundary atoms with increasing compression (figure 4(d)). Thus, the product of transition is mainly hcp phase in spite of some fcc atoms possibly existing during the transition under [001] compression. The homogeneous nucleation of the hcp phase can be seen from

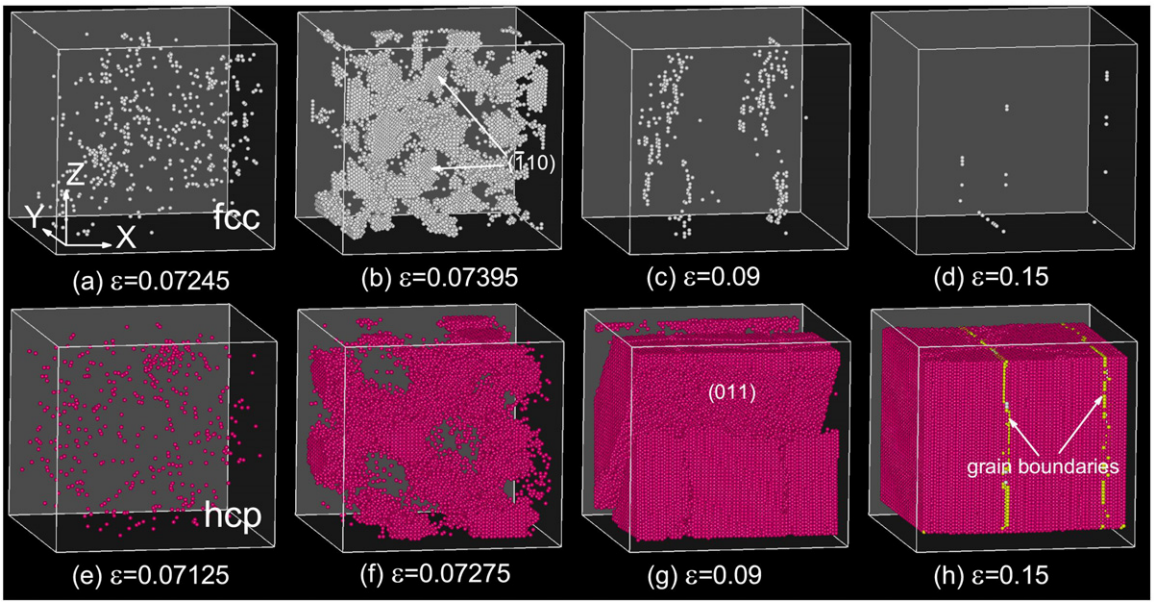

Figure 4. Morphology evolution of the fcc phase (the first row) and the hcp phase (the second row) in sample A. The coordinates are shown in panel (a) and the compression direction is along the Z axis. Color coding shows the topological medium-range-order analysis: white: fcc, red: hcp, yellow: grain boundaries.

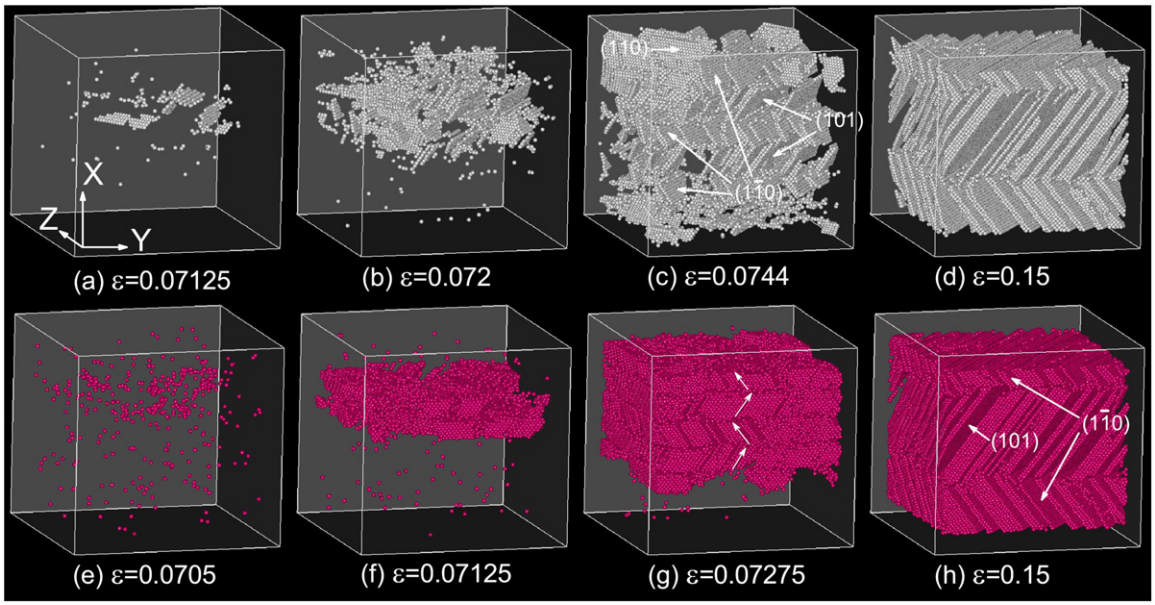

Figure 5. Morphology evolution of the fcc phase (the first row) and the hcp phase (the second row) in sample B. The coordinates are shown in panel (a) and the compression directions is along the X axis. The color coding is the same as figure 4.

figure 4(e), and the nuclei grow rapidly into irregular grains (figure 4(f)). These grains subsequently develop into the typical laminar structure along the $(011)_{bcc}$ planes, as shown in figure 4(g). Ultimately, the laminar structure grows into larger and regular grains divided by the grain boundaries (figure 4(h)). The grain boundary planes are $(100)_{bcc}$ planes, paralleling with the compression direction. Comparing with our previous study [18], the following prominent features can be seen: (i) the product of transition is mainly hcp phase with little fcc stacking faults both in current and previous studies. The typical laminar structure has been observed. However, the fcc phase is only a transient state in the current study, which has not been observed in previous static loading; (ii) when loading along other orientations (see further discussions below), homogeneous nucleation of the hcp and fcc phases and interaction between them are observed in present study. These observations are more complicated than those in [001] loading.

While loading along [011] (see figure 5), the fcc phase nucleates on $(110)_{bcc}$, $(101)_{bcc}$, and $(1\bar{1}0)_{bcc}$ planes and the hcp on $(101)_{bcc}$ and $(1\bar{1}0)_{bcc}$ planes. These nucleation planes all belong to the $\{110\}_{bcc}$ family. More specially, the fcc atoms first nucleate as a flaky structure (figure 5(a)), then, together

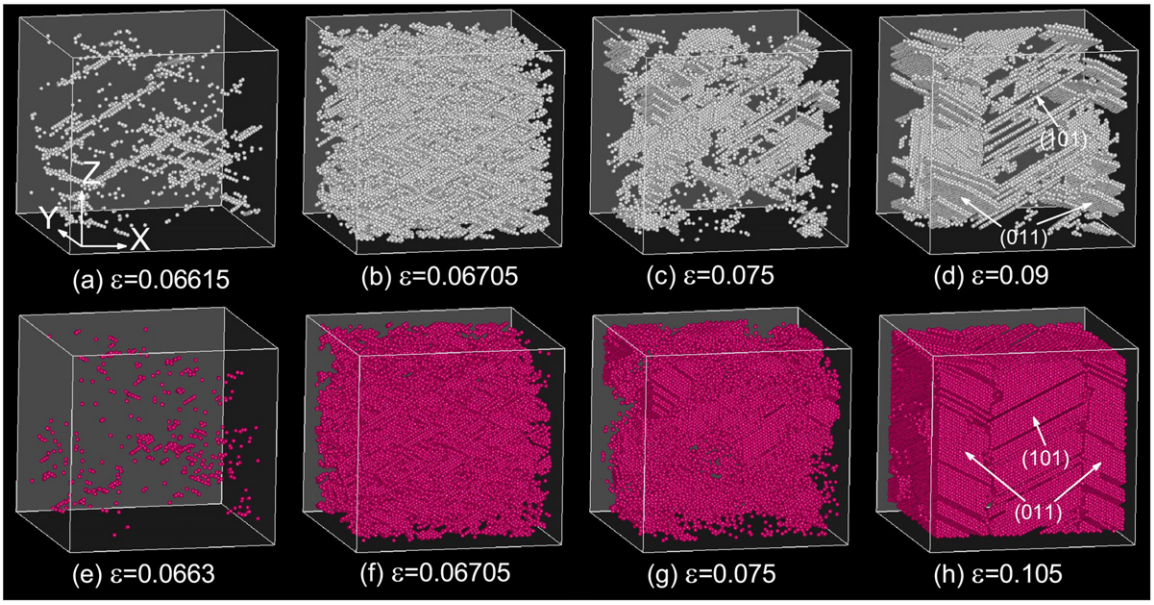

Figure 6. Morphology evolution of the fcc phase (the first row) and the hcp phase (the second row) in sample C. The coordinates are shown in panel (a) and the compression directions is along Z axis. The color coding is the same as figure 4.

with hcp atoms, evolve into the thin sandwich structure perpendicular to the compression direction (see figures 5(b), (c), (f), and (g)). At the end of loading, the fcc and hcp atoms form a stacking fault structure and a relatively thick sandwich structure (figures 5(d) and (h)). Therein, the sandwich structure is divided by the grain boundaries. Note that the grain boundary planes are $(011)_{\mathrm{bcc}}$ planes and perpendicular to the compression direction.

For loading along [111] (see figure 6), the nucleation and growth of the close packed phases are different. Just over the critical pressure, both fcc and hcp atoms nucleate to form lots of small but long flaky structure nuclei (figures 6(a), (b), (e), and (f)). From figure 3(c), a relaxation process right after the critical point $T_{\mathrm{s},[111]}$ has been observed. Although the fractions of fcc and hcp phases are reduced, the arrangement of atoms becomes more erratic, as shown in figures 6(c) and (g). At the end of loading, the stacking fault arrangement comes out in the interior of thick sandwich structure. Compared to the [011] loading, both fcc and hcp nucleation crystalline planes in [111] loading are $(101)_{\mathrm{bcc}}$ and $(011)_{\mathrm{bcc}}$. In addition, the grain boundary planes $(\bar{1}10)_{\mathrm{bcc}}$ in [111] loading are parallel, instead of perpendicular (in the case of [011] loading), to the compression orientation.

On the whole, for [001] loading, the bcc to hcp transition happens in the whole body of the sample and the fcc structure only appears as the intermediate structure. However, for [011] and [111] loadings, the fcc and hcp structures nucleate simultaneously. Note that for [011] loading the nucleation is localized. The hcp structure reaches its maximum at the evolved strain of ∼0.09 and ∼0.1 for [011] and [111] loadings, respectively. A further increase of strain will result in the decease (increase) of hcp (fcc) weight. A visible difference between [011] and [111] loadings is that for the latter there occurs an evident relaxation process after the critical point.

3.3. Radial distribution function analysis

The slip investigation of atoms must rely upon radial distribution function (RDF) analysis and phase mass fraction analysis. Figure 7 displays the RDFs under different compressions, where the strains of all three samples are from 0 to 0.15. The ideal positions of fcc and hcp structures have also been plotted. Along with the increase of strain the first peak in all three samples deviates towards the left gradually, while the second peak deviates towards the first peak and disappears finally. After the strain becomes larger than 0.0975, along with the disappearance of the second peak, a new peak appears, with the position (shown by the arrows in figure 7) exactly the same as that of the second peak of the fcc/hcp phases. Therefore, these changes in RDFs definitely signify atomic transformation to the close packed phases. Moreover, the evident broadening of the peaks in [011] and [111] loadings after transition is caused by the temperature effect. The third and fourth peaks at $\varepsilon = 0.15$ in figure 7(a) have an obvious trend to split; this is prominently different from that in figures 7(b) and (c). This further illustrates that sample A mainly features the hcp phase at the end of loading.

4. Conclusions

In summary, we have simulated the process of the bcc to hcp/fcc structural phase transition in bcc single crystal iron under uniaxial compression along three typical bcc orientations by MD method. It is found that samples B and C experience a more evident hardening process compared with sample A before phase transition. The temperatures for [011] and [111] loadings increase more highly than that for [001] loading. The mixed phase interval of sample B is much shorter than other two samples. The transition pressures are very near for all three samples with a value of ∼14 GPa, over which

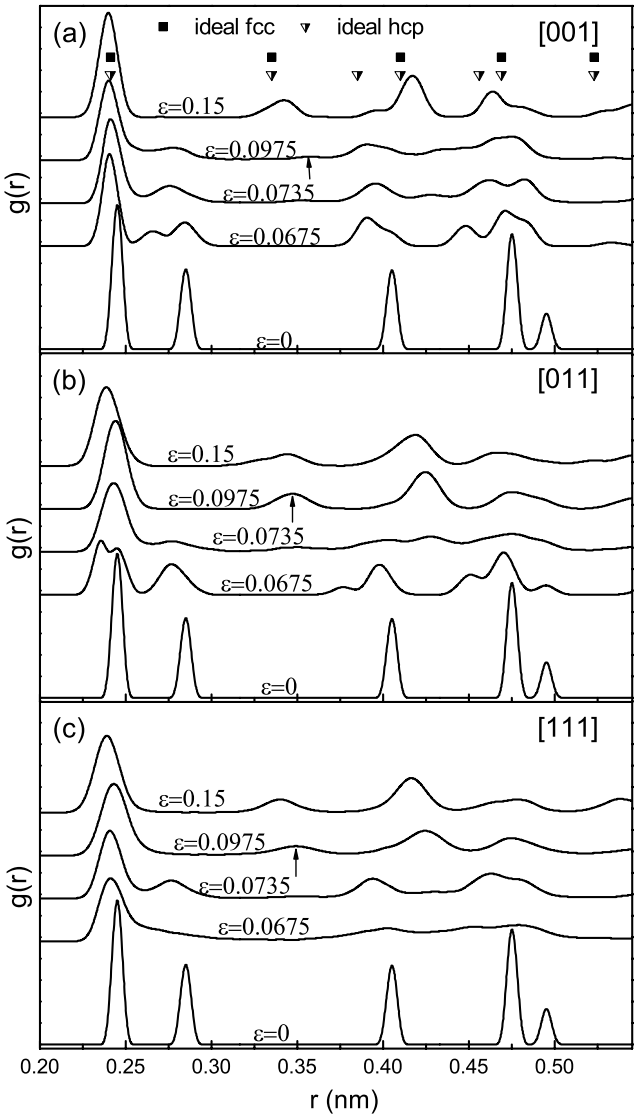

Figure 7. Radial distribution functions (RDFs) under different strains ε for loading along [001] (a), [011] (b), and [111] (c) directions. The ideal positions of the fcc and hcp structures, as well as the distribution function for the unstrained bcc ($\varepsilon = 0$), are also shown.

the nucleation of hcp and fcc atoms appears and grows into different morphologies. For [001] loading, the bcc to hcp/fcc transition happens in the whole body of the sample and hcp atoms nucleate on $(011)_{bcc}$ planes to form a laminar structure; the fcc phase only appears intermediately. For [011] and [111] loadings, however, (i) nucleation of fcc and hcp structures occurs simultaneously; (ii) the hcp mass fraction reaches its maximum at the evolved strain of ∼0.09 and ∼0.1 and any further increase of strain will result in a decrease (increase) of hcp (fcc) weight; (iii) the fcc and hcp atoms form a stacking fault structure and a relatively thick sandwich structure at the end of loading.

Acknowledgments

This study was supported by the Foundation for Development of Science and Technology of China Academy of Engineering Physics under Grant Nos 2008B0101008 and 2009A0102005.

References

[1] Bancroft D, Peterson E L and Minshall S 1956 *J. Appl. Phys.* **27** 291
[2] Jamieson J C and Lawson A W 1962 *J. Appl. Phys.* **33** 776
[3] Anderson O L 1985 *Nature* **314** 407
[4] Barker L M and Hollenbach R E 1974 *J. Appl. Phys.* **45** 4872
[5] Birch F 1952 *J. Geophys. Res.* **57** 227
[6] Taylor R D, Pasternak M P and Jeanloz R 1991 *J. Appl. Phys.* **69** 6126
[7] Hasegawa H and Pettifor D G 1983 *Phys. Rev. Lett.* **50** 130
[8] Boettger J C and Wallace D C 1997 *Phys. Rev.* B **55** 2840
[9] Wang F M and Ingalls R 1998 *Phys. Rev.* B **57** 5647
[10] Caspersen K J, Lew A, Ortiz M and Carter E A 2004 *Phys. Rev. Lett.* **93** 115501
[11] Kadau K, Germann T C, Lomdahl P S and Holian B L 2002 *Science* **296** 1681
[12] Daw M S and Baskes M I 1983 *Phys. Rev. Lett.* **50** 1285
[13] Daw M S and Baskes M I 1984 *Phys. Rev.* B **26** 6443
[14] Kalantar D H, Belak J F, Collins G W, Colvin J D, Davies H M, Eggert J H, Germann T C, Hawreliak J, Holian B L, Kadau K, Lomdahl P S, Lorenzana H E, Meyers M A, Rosolankova K, Schneider M S, Sheppard J, Stölken J S and Wark J S 2005 *Phys. Rev. Lett.* **95** 075502
[15] Kadau K, Germann T C, Lomdahl P S and Holian B L 2005 *Phys. Rev.* B **72** 064120
[16] Kadau K, Germann T C, Lomdahl P S and Holian B L 2007 *Phys. Rev. Lett.* **98** 135701
[17] Cui X, Zhu W, He H, Deng X and Li Y 2008 *Phys. Rev.* B **78** 024115
[18] Shao J L, Duan S Q, He A M, Qin C S and Wang P 2009 *J. Phys.: Condens. Matter* **21** 245703
[19] Harrison R, Voter A F and Chen S P 1989 *Atomistic Simulation of Materials* ed V Vitek and D J Srolovitz (New York: Plenum) p 219
[20] Hoffmann K H 1996 *Computational Physics* (Berlin: Springer) p 268
[21] Irving J H and Kirkwood J G 1950 *J. Chem. Phys.* **18** 817
[22] Allen M P and Tildesley D J 1987 *Computer Simulations of Liquids* (Oxford: Oxford University Press) p 46
[23] Swope W C, Andersen H C, Berens P H and Wilson K R 1982 *J. Chem. Phys.* **76** 637
[24] Honeycutt J D and Andersen H C 1987 *J. Phys. Chem.* **91** 4950
[25] Hawreliak J, Colvin J D, Eggert J H, Kalantar D H, Lorenzana H E, Stölken J S, Davies H M, Germann T C, Holian B L, Kadau K, Lomdahl P S, Higginbotham A, Rosolankova K, Sheppard J and Wark J S 2006 *Phys. Rev.* B **74** 184107